ROYAL SOCIETY
OF CHEMISTRY

Check for updates

Highly sensitive and reproducible SERS substrate based on ordered multi-tipped Au nanostar arrays for the detection of myocardial infarction biomarker cardiac troponin I†

Qing Xiang,[a] Hao Wang,[a] Shengdong Liu,[a] Yilong Zheng,[a] Shipan Wang,[b] Huanhuan Zhang, [ID] *[a] Yonggang Min [ID] *[a] and Yuguang Ma [ID] [c]

Acute myocardial infarction (AMI) is a severe cardiovascular disease, for which early diagnosis is critical for reducing mortality and improving patient outcomes. Cardiac troponin I (cTnI) is widely recognized as the "gold standard" biomarker for AMI due to its high specificity and sensitivity. The concentration of cTnI correlates directly with different stages of AMI. Therefore, the accurate detection of cTnI concentration is of paramount importance. However, the low concentration of cTnI in biological fluids requires ultrasensitive detection methods. In this study, we developed a sandwiched surface enhanced Raman scattering (SERS)-based biosensor composed of SERS-immune substrate, target antigen, and SERS nanotags and realized sensitive and accurate detection of cTnI. The SERS-immune substrate features an ordered, multi-tipped monolayer of Au nanostars fabricated using a three-phase interfacial self-assembly method and 4-(2-hydroxyerhyl)piperazine-1-erhanesulfonic acid (HEPES) buffer modification. Compared to Au nanosphere SERS substrates, the Au nanostar SERS substrates exhibited about a 3-fold increase in Raman enhancement and demonstrated good uniformity and batch stability. This novel SERS detection platform, leveraging dual plasmonic enhancement from both the SERS-immune substrate and SERS nanotags, achieves detection of cTnI with a limit of detection (LOD) as low as 9.09 pg mL^{-1} and a relative standard deviation (RSD) as low as 11.24%. Thus, the Au nanostar SERS substrates developed in this study demonstrate significant potential for rapid and accurate detection of cTnI.

Introduction

Cardiovascular diseases (CVD) are the leading cause of death worldwide. According to the World Health Organization (WHO), over 23.3 million people are projected to die from CVD annually by 2030.[1] Acute myocardial infarction (AMI), a clinical manifestation of CVD, is characterized by myocardial necrosis (cell death) resulting from prolonged ischemia and reduced cardiac blood supply. This condition leads to irreversible myocardial damage caused by hypoxia and is a leading cause of CVD-related mortality.[2] Therefore, early diagnosis is crucial for effective treatment of AMI patients.

Currently, the determination of AMI relies primarily on measuring the concentration of biomarkers in blood samples. The diagnosis of AMI depends on the detection of multiple biomarkers, including cardiac troponin T (cTnT), cardiac troponin I (cTnI), and creatine kinase MB (CK-MB).[3–5] Previous studies have demonstrated that although both cardiac troponins are closely related to CVD mortality, cTnI exhibits a higher correlation with AMI.[6] Therefore, cTnI is regarded as the "gold standard" for AMI diagnosis and is recommended as a Class I indication. In healthy individuals, cTnI levels are typically around 0.4 ng mL^{-1}, while levels exceeding 2.0 ng mL^{-1} are indicative of an increased risk of future cardiac events.[7] These events may include recurrent AMI, heart failure, cardiac arrest, or the need for cardiac surgery. Once AMI occurs, cTnI levels rise rapidly within 4 hours and remain in the blood for about 4–10 days.[8] Accurate quantification of cTnI levels and prompt diagnosis within this golden window can substantially enhance treatment efficacy and save lives.

Currently, various detection and quantification methods have been developed for different protein biomarkers of AMI, including enzyme-linked immunosorbent assay (ELISA), che-

[a]School of Materials and Energy, Guangdong University of Technology, Guangzhou, 510006, PR China. E-mail: hh_zhang@outlook.com, ygmin@gdut.edu.cn
[b]Guangdong Juhua Printing Display Technology Co., Ltd, Guangzhou, 510700, PR China
[c]Department of Materials Science and Engineering, South China University of Technology, Guangzhou 510641, PR China
†Electronic supplementary information (ESI) available. See DOI: https://doi.org/10.1039/d5an00171d

miluminescent immunoassay (CLIA), fluorescent immunoassay (FIA), electrochemical immunoassay, and surface-enhanced Raman scattering (SERS) techniques. ELISA offers several advantages, including good specificity, cost-effectiveness, and reproducibility.[9] However, its complexity, time consumption, limited sensitivity, and susceptibility to interference are significant limitations.[10] CLIA is widely used in clinical AMI detection due to its light source independence and broad dynamic range,[11,12] yet the relatively high costs of instruments and reagents are significant drawbacks.[13] FIA is preferred for AMI detection due to its non-destructive nature, high sensitivity, and ease of labeling.[14,15] However, fluorescence methods still face limitations such as high cost, poor photostability, and photobleaching.[16,17] Electrochemical immunoassay has advantages like good selectivity, simple equipment, and fast response.[18,19] However, its preparation process is complex and involves multiple sample handling steps, which can limit its widespread application in routine clinical settings.[20]

The SERS technique, characterized by its high sensitivity and non-destructive nature, provides a novel approach to overcome the limitations of traditional *in vitro* diagnostic methods such as fluorescence and chemiluminescence.[21,22] SERS-based biosensors offer several significant advantages: (1) Exceptional sensitivity: capable of detecting down to the single-molecule level. (2) Excellent selectivity: provides detailed molecular fingerprints through functionalization of SERS substrates with specific ligands, antibodies, or aptamers, enabling highly specific and selective binding to target molecules. (3) Multiplex detection: allows simultaneous detection of multiple analytes using a single excitation wavelength. (4) Minimal sample requirement: requires only trace amounts of samples, enabling rapid detection and facilitating emergency and on-site testing.[23] In recent years, SERS biosensors have been used for the detection and bioanalysis of various diseases, including different types of cancer,[24,25] neurodegenerative diseases,[26,27] cardiovascular diseases, infectious diseases, and parasitic infections.[28] As a powerful analytical tool, SERS shows great application potential in the field of biochemical detection and is expected to play a more critical role in future biomedical research and clinical diagnostics.[29–31]

To date, researchers have proposed various SERS probes and SERS immuno-substrates based on noble metal nanostructures for the detection of myocardial biomarkers. Cheng *et al.* used SERS immunoprobes (Au@Ag core–shell nanoparticles with bilayer MGITC as Raman reporter molecules) and gold array chips to achieve sensitive detection of cTnI and CK-MB, with limits of detection (LODs) estimated to be 8.9 pg mL^{-1} and 9.7 pg mL^{-1}, respectively.[32] Gao *et al.* developed a new plasmonic nanostripe microcone array substrate integrated microfluidic chip for the simultaneous SERS-based immunoassay of the CK-MB and cTnI cardiac markers. This chip achieved an impressively low LOD of 0.01 ng mL^{-1}.[33] Wang *et al.* used 5,5′-dithiobis-(2-nitrobenzoic acid)-labeled gold arrays as a SERS signal to effectively achieve signal self-calibration. In addition, an aptamer targeting cTnI and 4-mercaptobenzoic acid (4-MBA) as a secondary SERS signal were

anchored onto porous gold (pAu) to form a pAu-based signal probe. The resulting ratiometric aptasensor exhibited a low LOD down to 0.27 pg mL^{-1}.[34] Additionally, Lee *et al.* immobilized Raman reporter molecules Cy5 and aptamers with strong affinity for cTnI on gold nanoplates to prepare SERS aptamer probes for cTnI detection. By detecting the SERS signals of the sandwich immunoassay structure, they achieved LODs of 2.4 fg mL^{-1} and 2.4 pg mL^{-1} for cTnI in buffer solution and serum, respectively.[35] These results clearly demonstrate that SERS biosensors based on immunorecognition or aptamer recognition exhibit extremely high sensitivity in cTnI detection, highlighting their significant technical advantages.

In SERS-based immunoassays, the Raman scattering signals of reporter molecules are significantly enhanced at SERS-active sites, commonly referred to as "hot spots".[36] The formation of these "hot spots" is closely related to the size, shape, and arrangement of the nanoparticles on the substrate.[37] Therefore, constructing substrates with high-density and high-enhancement SERS "hot spots" is crucial for achieving excellent SERS performance.[38] Among all the fabrication techniques, solid-state SERS substrates fabricated using self-assembly techniques offer several key advantages, including uniformity, stability, and portability. Moreover, they enable large-area production, making them the most widely used SERS substrates to date. Common self-assembly methods include chemical adsorption, physical adsorption, and interfacial self-assembly. Chemical adsorption self-assembly is a technique that forms ordered films spontaneously through chemical bonding based on intermolecular interactions.[39] Physical adsorption self-assembly utilizes electrostatic interactions to uniformly assemble nanoparticles onto the substrate surface.[40] However, both methods have high requirements for the micromorphology and surface properties of the substrate and face limitations in constructing dense and ordered nanoarrays. The random distribution of substrate-loaded Au or Ag nanoparticles leads to poor reproducibility, which poses a major challenge to the performance and application of SERS substrates.

In contrast, interfacial self-assembly is straightforward and operationally simple. The resulting substrates exhibit dense nanoparticle compositions, with nanoscale gaps between nanoparticles serving as highly sensitive SERS "hot spots" that are uniformly distributed.[41] Therefore, monolayers of nanoparticles assembled by interfacial self-assembly are considered one of the most promising SERS substrates. However, preloaded noble metal nanoparticles, such as gold nanoparticles, are challenging to grow continuously on substrates using traditional room-temperature growth processes and common reducing agents like ascorbic acid to form nanostructures with controlled shapes. To date, devising an effective strategy that can preserve the initial arrangement of seed particles while enabling their controllable growth into morphologically diverse, substrate-supported nanoparticles remains a significant challenge in the field of nanotechnology.[42]

In this work, we developed a SERS biosensor featuring multiple "hot spots" for the quantitative detection of cTnI. As
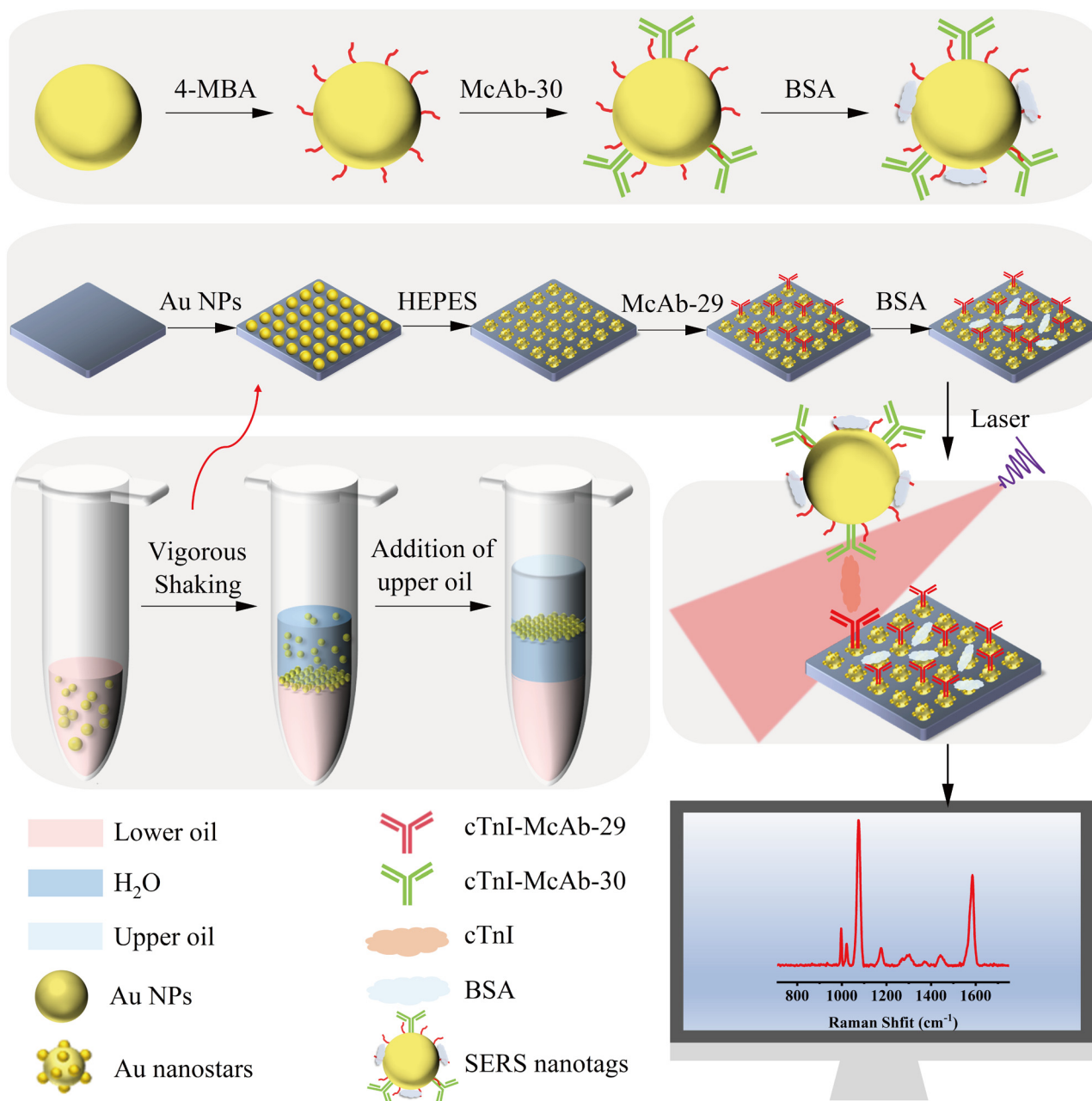
Fig. 1 Schematic diagram of the preparation process of the SERS-active immunoassay biosensor.

shown in Fig. 1, we first constructed an ordered, multi-tipped monolayer of Au nanostars as the SERS substrate using a three-phase interfacial self-assembly method.[43] Subsequently, the primary antibody was immobilized on the SERS substrate *via* 11-mercaptoundecanoic acid (11-MUA). Then, we used 4-MBA as the Raman reporter molecule to label Au nanoparticles (Au NPs) as SERS nanotags for antigen recognition. When the target antigen is present in the sample, a sandwich immunoassay structure is formed among the SERS-immune substrate, target antigen, and SERS nanotags. Finally, the target antigen is detected through the SERS signal of the 4-MBA Raman reporter molecule. This novel SERS detection

platform, leveraging dual plasmonic enhancement from both the substrate and SERS nanotags, achieves detection of cTnI with a LOD as low as 9.09 pg mL^{-1} and a relative standard deviation (RSD) as low as 11.24%.

Materials and methods

Materials

Chloroauric acid (HAuCl$_4$), polyvinyl pyrrolidone (PVP), 11-mercaptoundecanoic acid (11-MUA), cetyltrimethyl-ammonium chloride (CTAC), bovine serum albumin (BSA) and

4-(2-hydroxyerhyl)piperazine-1-erhanesulfonic acid (HEPES) were purchased from Sigma-Aldrich. Ascorbic acid (AA) was purchased from Sinopharm Chemical Reagent Co. 4-Mercaptobenzoic acid (4-MBA), sodium borohydride ($NaBH_4$), cetyltrimethylammonium bromide (CTAB), 1-ethyl-(3-dimethylaminopropyl) carbodiimide (EDC) and N-hydroxysuccinimide (NHS) were purchased from Aladdin Reagent Co., Ltd. Hexane and dichloromethane were purchased from Macklin Chemical. Reagent Co. Phosphate-buffered saline (PBS) was purchased from White Shark Biotechnology Co. cTnI-Ag5, cTnI-McAb-29 and cTnI-McAb-30 were purchased from Fapon Biotech Inc. Alpha fetoprotein (AFP) was purchased from ANEWBiosystems. All water used in experiments was ultrapure water.

Instruments

Scanning electron microscope (SEM) images were obtained by field emission scanning electron microscopy (Hitachi, SU8100) under accelerating voltage conditions of 5.0 kV. Ultraviolet-visible absorption (UV-vis) spectra were recorded using a microplate reader (BioTek, 800 TS). Size distribution maps and zeta potential maps were obtained using a multi-angle particle size and high-sensitivity zeta potential analyzer (Brookhaven Instruments Corporation, Omni). Raman spectra were obtained by a Raman spectrometer (Renishaw, inVia™ confocal Raman microscope) using a 785 nm excitation laser and a 50× objective lens. The laser power was 10%, the integration time was 5 s, and all spectra were baseline corrected.

Synthesis of Au nanopolyhedra

Au nanopolyhedra of various sizes were synthesized using a seed-mediated growth method.[44] Initially, $HAuCl_4$ (10 mM, 0.25 mL) and CTAB (0.1 M, 9.75 mL) were vigorously stirred and mixed, followed by the rapid addition of freshly prepared $NaBH_4$ (0.01 M, 0.60 mL). After the reaction was complete, CTAB-capped gold clusters were obtained. Subsequently, CTAC (0.2 M, 2 mL), AA (0.1 M, 1.5 mL), and 50 μL of the CTAB-capped gold cluster solution were sequentially added to a beaker and mixed, followed by a one-time injection of $HAuCl_4$ aqueous solution (0.5 mM, 2 mL). The reaction was carried out at room temperature for 15 minutes to obtain 10 nm Au nanosphere seed solution. Finally, CTAC (0.1 M, 20 mL), AA (0.01 M, 1.3 mL), and 400 μL of the 10 nm seed solution were mixed, and then $HAuCl_4$ aqueous solution (0.5 mM, 20 mL) was slowly injected. After the injection, the reaction was allowed to proceed at room temperature for 10 minutes. The reaction mixture was then centrifuged at 8000 rpm for 10 minutes and re-dispersed in CTAB solution (0.02 M, 40 mL) to obtain Au nanopolyhedra.

Synthesis of Au NPs

Au NPs were prepared by oxidizing Au nanopolyhedra with $HAuCl_4$ aqueous solution.[45] In a constant temperature water bath at 40 °C, $HAuCl_4$ aqueous solution (5 mM, 0.4 mL) was added to the Au nanopolyhedron solution and gently stirred for 0.5 hours. After the reaction was complete, the resulting Au NPs were centrifuged (8000 rpm, 10 min) and re-dispersed in water for storage.

Preparation of SERS nanotags

SERS nanotags were prepared using the aforementioned Au NPs. First, Au@4MBA was obtained by adding 4-MBA ethanol solution (0.1 mM, 80 μL) to the Au NP solution (4 mL), stirring overnight, and then centrifuging at 8000 rpm for 10 minutes. Subsequently, 50 μL of cTnI-McAb-30 antibody solution (25 μg mL^{-1}) was added to the Au@4-MBA and incubated at 4 °C for 6 hours. After incubation, the mixture was centrifuged at 6500 rpm for 10 minutes and then blocked with 4 mL of PBS buffer containing 0.1% BSA to obtain the SERS nanotags. The prepared SERS nanotags were stored in the refrigerator at 4 °C for later use.

Preparation of Au nanosphere arrays

Au nanosphere arrays were assembled on hydrophilic silicon wafers treated with Piranha solution using an oil/water/oil three-phase liquid–liquid interfacial self-assembly method.[43] First, the hydrophilic surface ligand CTA$^+$ on Au NPs (40 mL) was replaced with PVP by adding PVP ethanol solution (1 wt%). The PVP-protected Au NPs were then centrifuged at 8000 rpm for 10 minutes, and the resulting precipitate was re-dispersed in 4 mL of ethanol. Next, 0.40 mL of the PVP-coated Au NPs dispersion was mixed with 1 mL of dichloromethane, followed by the addition of 1.6 mL of water. The mixture was vigorously shaken for 1 minute to form a yellow film at the dichloromethane/water interface. Then, 400 μL of n-hexane was slowly added along the wall of the centrifuge tube. After slightly tilting and rotating the centrifuge tube, the Au NPs were transferred to the n-hexane/water interface, forming a metallic luster monolayer film. The upper n-hexane layer was removed with a pipette, and after the n-hexane completely evaporated, the Au NPs were transferred onto the pre-treated hydrophilic silicon wafer. Finally, Au nanosphere arrays were obtained.

Preparation of Au nanostar arrays

The modification process with HEPES buffer referenced previous work.[46] The Au nanosphere array was immersed in a mixture of HEPES solution (75 mM, 30 mL) at pH 7.4 and $HAuCl_4$ aqueous solution (25 mM, 0.61 mL) in an ice bath at 10 °C for 1.5 h and 3 h to grow short branches. After washing three times with ultrapure water and drying, Au nanostar arrays were obtained.

Preparation of the SERS-immune substrate

The SERS immuno-substrate was prepared by modifying the Au nanostars surface with primary antibodies. The Au nanostar array was soaked in a 20 μM 11-MUA ethanol solution overnight and then rinsed three times with ethanol. EDC (10 μL, 25 mM) and NHS (10 μL, 25 mM) were dropped onto each silicon wafer and incubated for 30 minutes to activate the carboxyl groups. Then, 50 μL of cTnI-McAb-29 antibody solution (25 μg mL^{-1}) was dropped onto the substrate and incubated at 37 °C for 4 hours. Unbound antibodies were removed with PBS buffer. Finally, 50 μL of BSA solution (5% w/v) was

dropped onto the substrate and incubated at 37 °C for 1 hour to block excess active sites. Excess BSA was removed with PBS buffer, yielding the cTnI-McAb-29 antibody-modified SERS immuno-substrate, which was stored at 4 °C for later use.

Sandwich immunoassay

To quantify cTnI, the cTnI-Ag5 protein was first diluted to various concentrations. Then, 50 μL of each diluted antigen sample was dropped onto the SERS immuno-substrate and incubated at 37 °C for 2 hours. The substrate was then rinsed three times with PBS buffer. Next, 50 μL of the SERS nanotags was added to the substrate and incubated at 37 °C for 2 hours to form the sandwich immunoassay structure. Finally, after rinsing the substrate with PBS buffer, it was stored at 4 °C for subsequent detection.
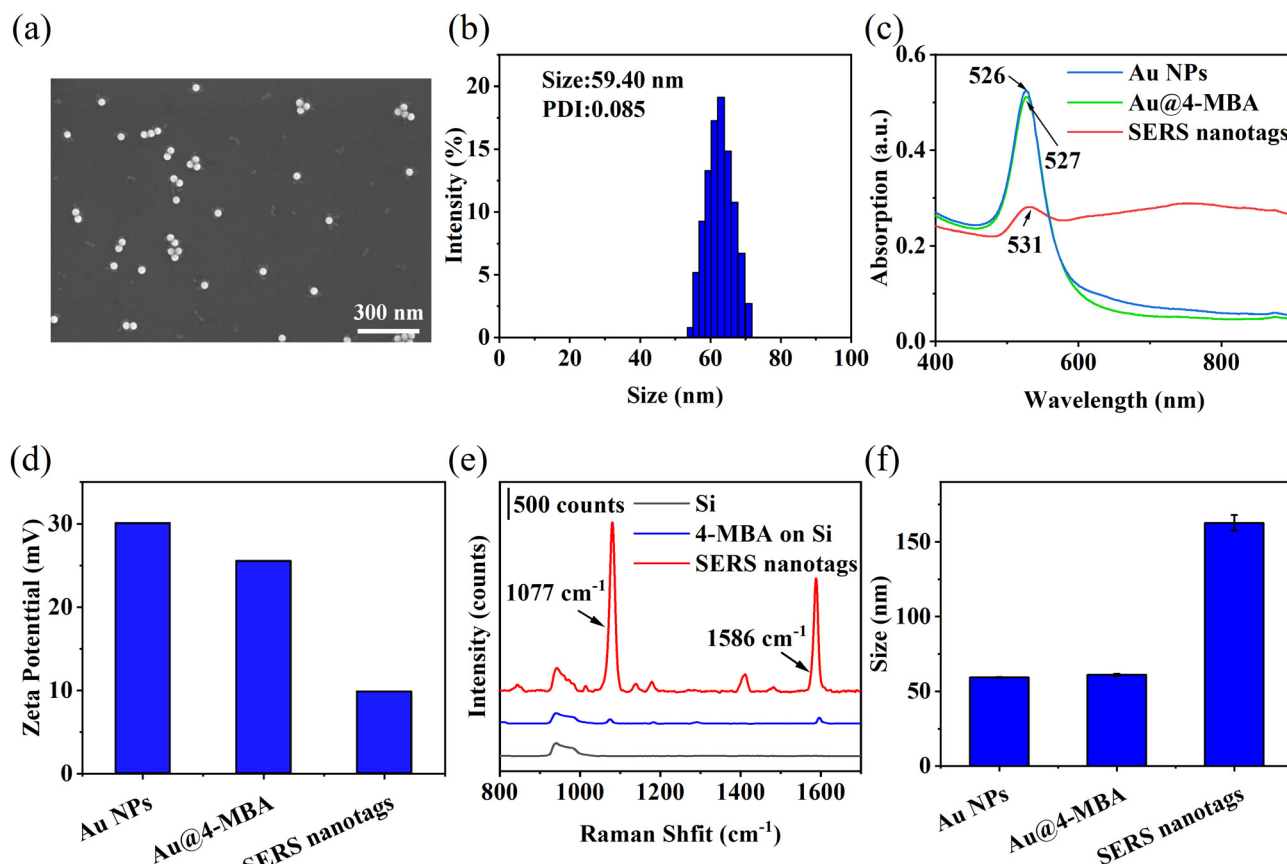
Results and discussion

Preparation and characterization of SERS nanotags

Au nanopolyhedra were synthesized *via* a seed-mediated method.[44] The SEM image of the prepared Au nanopolyhedra shown in Fig. S1† reveals a polyhedral shape with relatively sharp vertices and edges. The polydispersity index (PDI) was 0.226 (Fig. S2†), indicating an initially non-uniform size distribution. Previous work has shown that mild oxidation can effectively reshape gold nanocrystals, enabling precise control of their shape and size.[45] This process selectively etches high-curvature surface sites, which is particularly beneficial for the preparation of Au nanospheres. Based on this principle, we transformed Au nanopolyhedra into spherical structures through a mild oxidation process. The color change observed in the etched Au NP solution (Fig. S3†) indicates a change in the surface morphology of the Au nanopolyhedra, which leads to altered optical properties. Further SEM analysis revealed that the etched nanoparticles exhibited a spherical shape with a smooth surface (Fig. 2(a)). Size distribution analysis further confirmed that, compared to the unetched Au nanopolyhedra, the etched nanoparticles had a narrower size distribution (PDI = 0.085), indicating a more uniform size distribution with an average size of approximately 59.40 nm (Fig. 2(b)). Thus, Au NPs with a size of 59.4 nm were successfully obtained.

During the synthesis of SERS nanotags, UV-vis spectra of Au NPs at different stages were measured to monitor the surface modification process (Fig. 2(c)). The as-prepared Au NPs exhibited a strong UV absorption peak at 526 nm. Upon

Fig. 2 (a) SEM image of Au NPs. (b) Particle size distribution of Au NPs. (c) UV-vis absorption spectra of Au NPs, Au@4-MBA, and SERS nanotags. (d) Zeta potentials of Au NPs, Au@4-MBA, and SERS nanotags. (e) SERS spectra of 4-MBA and SERS nanotags. (f) Hydrated particle size of Au NPs, Au@4-MBA, and SERS nanotags.

modification with the Raman reporter molecule 4-MBA, the peak slightly red-shifted to 527 nm. Further mixing with the cTnI-McAb-30 antibody solution led to a significant red shift from 527 nm to 531 nm, confirming the successful anchoring of cTnI-McAb-30 on Au NPs@4-MBA.[47] Meanwhile, the changes in the zeta potential also verified the successful conjugation of 4-MBA and cTnI-McAb-30 on Au NPs (Fig. 2(d)). The zeta potential of Au NPs shifted from 30.80 mV to 25.53 mV following the coupling of 4-MBA. This change is attributed to the formation of Au–S bonds between the thiol group (–SH) in 4-MBA and the Au NPs. This interaction alters the surface charge. Additionally, the carboxyl group (–COOH) in 4-MBA ionizes in aqueous solution to form negatively charged carboxylate ions. These ions neutralize some of the positive charges on the Au NPs, thereby reducing the overall zeta potential. After incubation with cTnI-McAb-30, the zeta potential further decreased to 9.85 mV. This suggests that the binding of the antibody likely covers the original positive surface charges, reducing their exposure and thereby further lowering the zeta potential. Furthermore, the presence of 4-MBA was confirmed by the appearance of its characteristic Raman peaks at 1077 cm^{-1} and 1586 cm^{-1} observed in the Raman spectra (Fig. 2(e)). These peaks are attributed to the in-plane ring breathing mode ν(C–S) and aromatic ring ν(C–C) vibration modes, respectively.[48] This further verifies the successful synthesis of the SERS nanotag. Notably, the Raman signal of the SERS nanotag was significantly stronger than that of 4-MBA of the same concentration on bare Si, which served as a control. This enhanced signal suggests the presence of the locally enhanced electromagnetic field on the Au NPs surface.
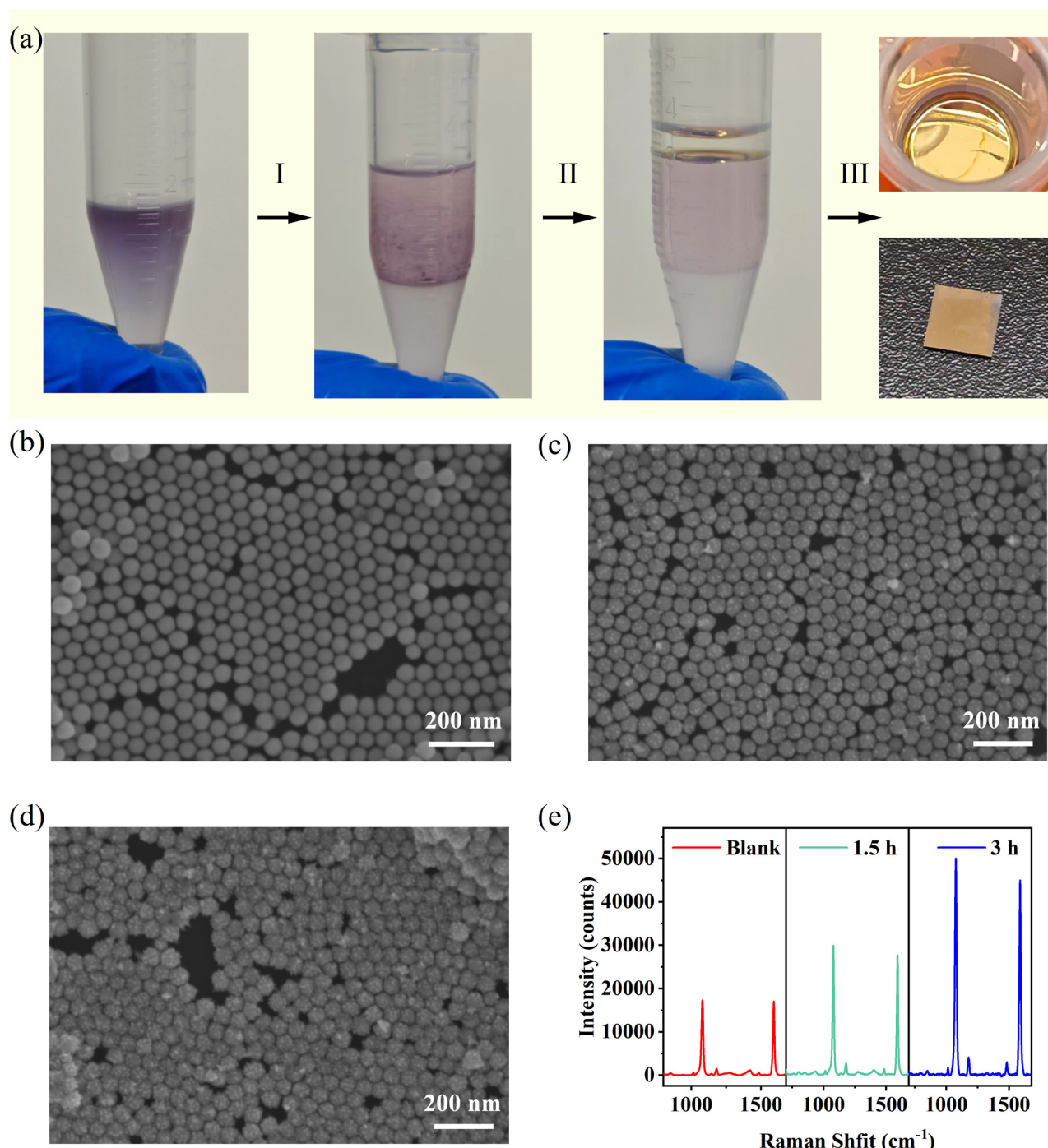
The particle size of the SERS nanotag was characterized by the dynamic light scattering instrument (Fig. 2(f)). The particle size increased from 59.4 nm to 61.07 nm after Au NPs were combined with 4-MBA and further increased to 162.78 nm after the incubation with cTnI-McAb-30 (Fig. S4†). After the 4-MBA molecules attached to the Au NPs, the increased surface hydrophobicity led to a tendency for aggregation.[49] Additionally, slight aggregation may also occur during the multiple processing steps of the SERS nanotags, such as reagent addition, continuous purification, and centrifugation.[50] As a result, the size of the SERS nanotag is significantly larger than that of the bare Au NPs. Meanwhile, the SEM image of the SERS nanotags also confirmed their successful preparation (Fig. S5†).

Preparation and optimization of SERS-immune substrate

The reproducibility of SERS substrates is crucial for the accuracy and reliability of SERS immunoassays. Traditional methods of chemical and physical adsorption self-assembly not only involve time-consuming preparation processes, but also lead to random distribution of Au or Ag nanoparticles on substrates, which results in poor reproducibility of detected signals. Herein, we used etched Au NPs with an average size of 59.4 nm (Fig. 2(a)) to fabricate Au nanosphere arrays *via* a Marangoni effect-driven three-phase self-assembly method.[43] Initially, an ethanol solution of Au NPs was mixed with di-

chloromethane and water. After vigorous shaking for 1 minute, a non-close-packed golden film was obtained at the dichloromethane/water interface (process I in Fig. 3(a)). Subsequently, n-hexane was carefully added along the wall of the centrifuge tube, and the tube was gently rotated. This resulted in a dense monolayer of Au NPs at the n-hexane/water interface (process II in Fig. 3(a)). After the upper oil phase was removed, the monolayer of Au NPs was transferred onto a silicon wafer that had been treated to be hydrophilic to obtain an Au nanosphere array (process III in Fig. 3(a)). SEM results revealed significant differences between the etched Au nanosphere array (Fig. 3(b)) and the unetched Au nanopolyhedron monolayer (Fig. S6†). The Au nanosphere array exhibited a highly uniform arrangement with no obvious aggregation or large gaps, achieving a coverage rate approaching 100% (Fig. S7†). In contrast, the monolayer of unetched Au nanopolyhedra showed inconsistent particle shapes and noticeable gaps. This significant difference arises from the key role of the non-template-guided self-assembly process. In this process, various non-covalent interactions between nanoparticles, such as van der Waals forces and Coulomb forces,[51,52] as well as external fields (such as electric, magnetic, and flow fields),[53] are crucial for guiding disordered suspended particles into ordered structures. Moreover, the uniform size and morphology of nanoparticles are of paramount importance, as these homogeneous particles serve as the fundamental building blocks for constructing ordered nanostructures.[54] This uniformity and compactness are essential for creating efficient SERS-active substrates, as they directly affect the distribution and density of "hot spots", thereby influencing the reproducibility of SERS signals.

It is widely recognized that the significant enhancement of SERS signals of noble metal nanostructures is primarily attributed to the localized surface plasmonic resonance (LSPR).[55] The highest LSPR intensities primarily occur in narrow spatial regions, such as tips, particle gaps, and the interfaces between particles and substrates—areas commonly referred to as "hot spots". It has been reported that Au nanostars with sharp tips can generate stronger LSPR compared to other shapes, such as Au nanospheres, nanorods, nanotriangles, and nanobipyramids.[56] Therefore, we transformed the substrate-supported monolayer of Au nanospheres into an ordered monolayer of multi-tipped Au nanostars through HEPES buffer modification. The alkanesulfonate group in HEPES has been proposed to promote the anisotropic growth of branches.[57] This approach enabled the construction of a highly sensitive SERS substrate. We optimized the soaking time of HEPES buffer on the surface of Au nanospheres. As shown in Fig. 3(c), after soaking in HEPES buffer for 1.5 hours, short spines were clearly observed on the surface of Au nanospheres. With the soaking time reaching 3 hours, the number of short spines significantly increased, and the surface of nanoparticles became rougher (Fig. 3(d)), while the nanoparticles still maintained a highly ordered array structure. This indicates that during the morphological evolution, the relative positions and arrangement patterns of the particles were well preserved.
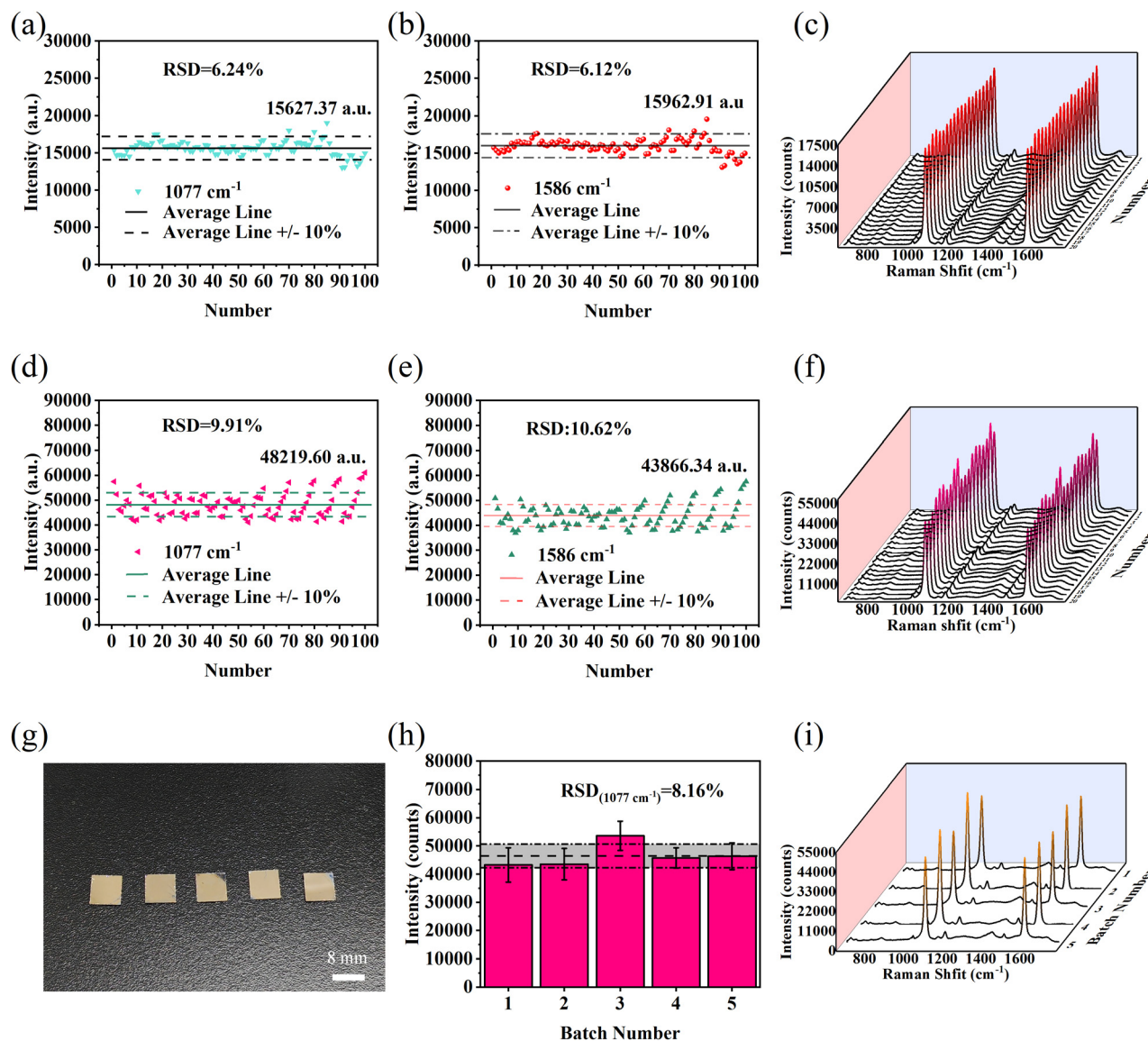
Fig. 3 (a) Photographs of the three-phase self-assembly process for preparing the Au nanosphere array (I: vigorously shaking, II: adding *n*-hexane, III: transfer of Au nanosphere array on silicon wafer). (b) SEM image of the Au nanosphere array. (c) SEM image of the Au nanostar array after HEPES buffer soaking for 1.5 hours. (d) SEM image of the Au nanostar array after HEPES buffer soaking for 3 hours. (e) Raman intensity of 4-MBA (10^{-4} M) obtained from three different arrays.

Additionally, the Au nanostar array obtained after soaking in HEPES buffer for 3 hours exhibited significantly stronger enhancement for 4-MBA compared to the other two and was therefore selected for subsequent performance analysis and Raman immunoassay (Fig. 3(e)).

To verify the morphology-related SERS performance, the Raman spectra of the reporter molecule 4-MBA were collected at 100 random points both on the Au nanosphere and Au nanostar substrates. As shown in Fig. 4(a), (b), and (c), for the Au nanosphere array, the Raman intensity of the characteristic

Fig. 4 (a) Raman intensity of characteristic peaks at 1077 cm^{-1} and (b) 1586 cm^{-1} for 4-MBA (10^{-4} M) on Au nanosphere array. (c) Raman spectra from 20 random spots on Au nanosphere array. (d) Raman intensity of characteristic peaks at 1077 cm^{-1} and (e) 1586 cm^{-1} for 4-MBA (10^{-4} M) on Au nanostar array. (f) Raman spectra from 20 random points on Au nanostar array. (g) Photograph of five different batches of Au nanostar arrays on Si wafers with each size of 0.8 × 0.8 cm^2. (h) Raman intensity at peak 1077 cm^{-1} and (i) Raman spectra of 4-MBA (10^{-4} M) obtained from five different batches of Au nanostar arrays.

peaks at 1077 cm^{-1} and 1586 cm^{-1} exhibited low RSD of 6.24% and 6.12%, respectively, indicating good uniformity and high reproducibility. As for the Au nanostar array, as shown in Fig. 4(d), (e), and (f), the RSD of the Raman intensity of the characteristic peaks at 1077 cm^{-1} and 1586 cm^{-1} were 9.91% and 10.62%, respectively. The decrease in substrate uniformity is attributed to the fact that HEPES reduces Au^{3+} to achieve the seedless synthesis of Au nanostars, and a small amount of Au nanostars remain on the substrate after immersion, resulting in slightly higher local signals during Raman detection. However, this has no significant interference with the experimental results. The intensity of the characteristic peaks in the Au nanostar array was significantly higher than that in the Au

nanosphere array. The peak intensity of the Au nanostar array at 1077 cm^{-1} was calculated to be 3.08 times of that on the Au nanosphere array. This enhancement is attributed to the generation of short branches on the surface of the nanoparticles, which create more "hot spots" to enhance the SERS signal. To further verify the enhancement performance of the prepared substrate, the enhancement factor (EF) was calculated using the equation: EF = $(I_{\text{SERS}}/C_{\text{SERS}})/(I_{\text{Raman}}/C_{\text{Raman}})$, where I and C represent the signal intensity at 1077 cm^{-1} and the concentration of 4-MBA, respectively. As shown in Fig. S8,† the EF of the prepared Au nanostar array was calculated to be 2.11 × 10^5, which is comparable to those reported for similar array substrates.[58]

To further evaluate the reproducibility of the Au nanostar array, we investigated the SERS performance of different batches of substrates to assess the batch consistency. Five batches of Au nanostar arrays were transferred onto silicon wafers with a size of 0.8×0.8 cm^2 (Fig. 4(g)). These wafers were then soaked in a 0.1 mM 4-MBA ethanol solution for 2 hours. SERS spectra from 100 random points on each substrate were collected. The RSD of the SERS intensities at 1077 cm^{-1} and 1586 cm^{-1} for the five batches were 8.16% and 8.18%, respectively (Fig. 4(h) and Fig. S9†), indicating excellent batch uniformity (Fig. 4(i)).
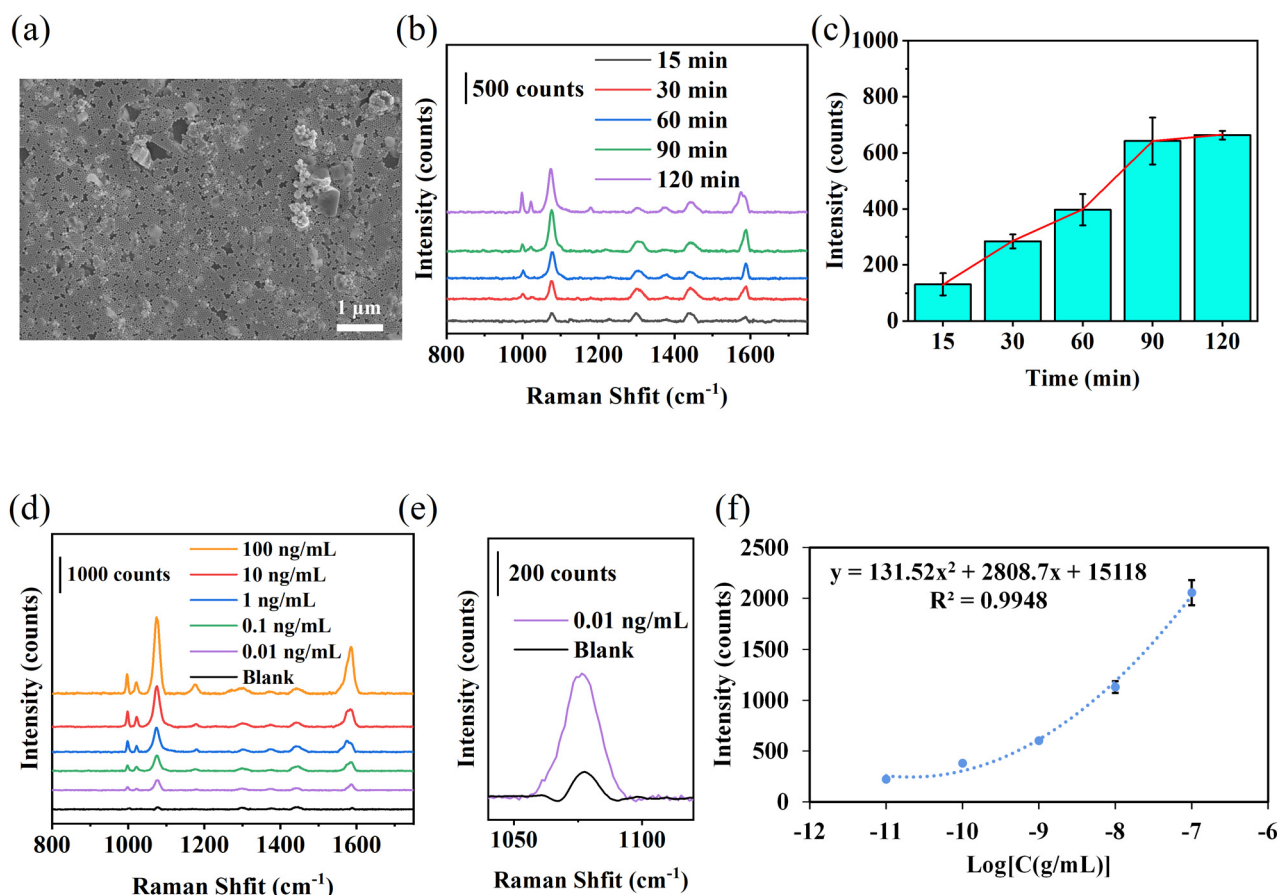
Performance of the SERS sensor for cTnI detection

Further, the performance of the prepared SERS sensor for AMI biomarker detection was thoroughly investigated. First, the cTnI-McAb-29 antibody was immobilized on the SERS-active substrate. Subsequently, antigen proteins and SERS nanotags were sequentially incubated on the SERS immuno-substrate to form a sandwich structure through specific antigen–antibody binding. The morphological change of the SERS substrate after immune binding was observed using SEM. As shown in Fig. 5(a), compared to the unincubated SERS immuno-substrate (Fig. S7†), the surface of the incubated substrate showed significant changes, including the appearance of new nanostructures and increased surface coverage. Many small spherical structures could be seen on the chip substrate, consistent in size and shape with the SERS nanotags, indicating that the SERS nanotags were successfully adsorbed onto the SERS immuno-substrate through specific antigen–antibody reactions (Fig. S10†). Thus, a sandwich immunoassay structure was successfully constructed.

Before quantitative analysis of cTnI, we optimized the incubation time of SERS nanotags to maximize signal intensity. As the incubation time of SERS nanotags increased, the intensity of the 4-MBA characteristic peaks gradually increased, reaching a plateau at 90 min and stabilizing at 120 min (Fig. 5(b) and (c)). Therefore, the optimal incubation time for SERS nanotags was determined to be 120 min.

Under optimal experimental conditions, the quantitative capability of the prepared SERS sensor was verified by incubating different concentrations of target antigens on the SERS immuno-substrate. The Raman peak intensity at 1077 cm^{-1}, corresponding to the reporter molecule 4-MBA, was recorded to monitor the concentrations of cTnI. A control experiment was conducted without adding any antigen in the SERS immunoassay. As shown in Fig. 5(d), within the concentration

Fig. 5 (a) SEM image of the SERS substrate after immune reaction binding at a cTnI concentration of 100 ng mL^{-1}. (b) Raman spectra and (c) peak intensity at 1077 cm^{-1} for different incubation times. (d) Raman spectra of different concentrations of cTnI. (e) Enlarged Raman spectra at a concentration of 0.01 ng mL^{-1} and the blank sample in (d). (f) Calibration curve of the peak intensity at 1077 cm^{-1}.

range of 0.01 ng mL^{-1} to 100 ng mL^{-1}, the SERS signal increased continuously with the increasing concentration of the target antigen. Notably, the characteristic peak of 4-MBA could be detected even at a low concentration of 0.01 ng mL^{-1} (Fig. 5(e)). A calibration curve (Fig. 5(f)) was constructed by plotting the SERS intensity of the characteristic peak at 1077 cm^{-1} against the logarithm of cTnI concentration, yielding a correlation coefficient (R^2) of 0.9948. The error bars in the figure represent the standard deviation of five replicate measurements. The detection limit of cTnI was calculated using the International Union of Pure and Applied Chemistry (IUPAC) standard method (LOD = y_{blank} + 3 × SD$_{blank}$, where y_{blank} is the average value of the blank signal and SD$_{blank}$ is the standard deviation of the blank sample signal),[59] resulting in a LOD of 9.09 pg mL^{-1}. The sensitivity of our SERS detection method is on par with that of the previously reported works, which enables it to fulfill most practical detection requirements (Table S1†).

Reproducibility and specificity of SERS sensors

The reproducibility and specificity of SERS sensors are crucial for their accurate detection of targets in complex samples. The reproducibility of the SERS biosensor was examined by measuring the Raman spectra at 15 random locations on the sandwich immunoassay structure. As shown in Fig. 6(a) and (b), the RSD of the Raman intensity of the characteristic peak at 1077 cm^{-1} was 11.24%. The reproducibility of the SERS immunoassay platform was slightly lower than that of the Au nanostar array on the Si wafer. This is attributed to the non-uniform distribution or aggregation of SERS nanotags after multiple purification and centrifugation steps. However, compared to other reported SERS immunoassay platforms (10.29%),[60] our results showed comparable reproducibility, indicating the reliability of our SERS sensor in practical applications. Additionally, our SERS substrate demonstrates reasonable stability under ambient temperature storage conditions,
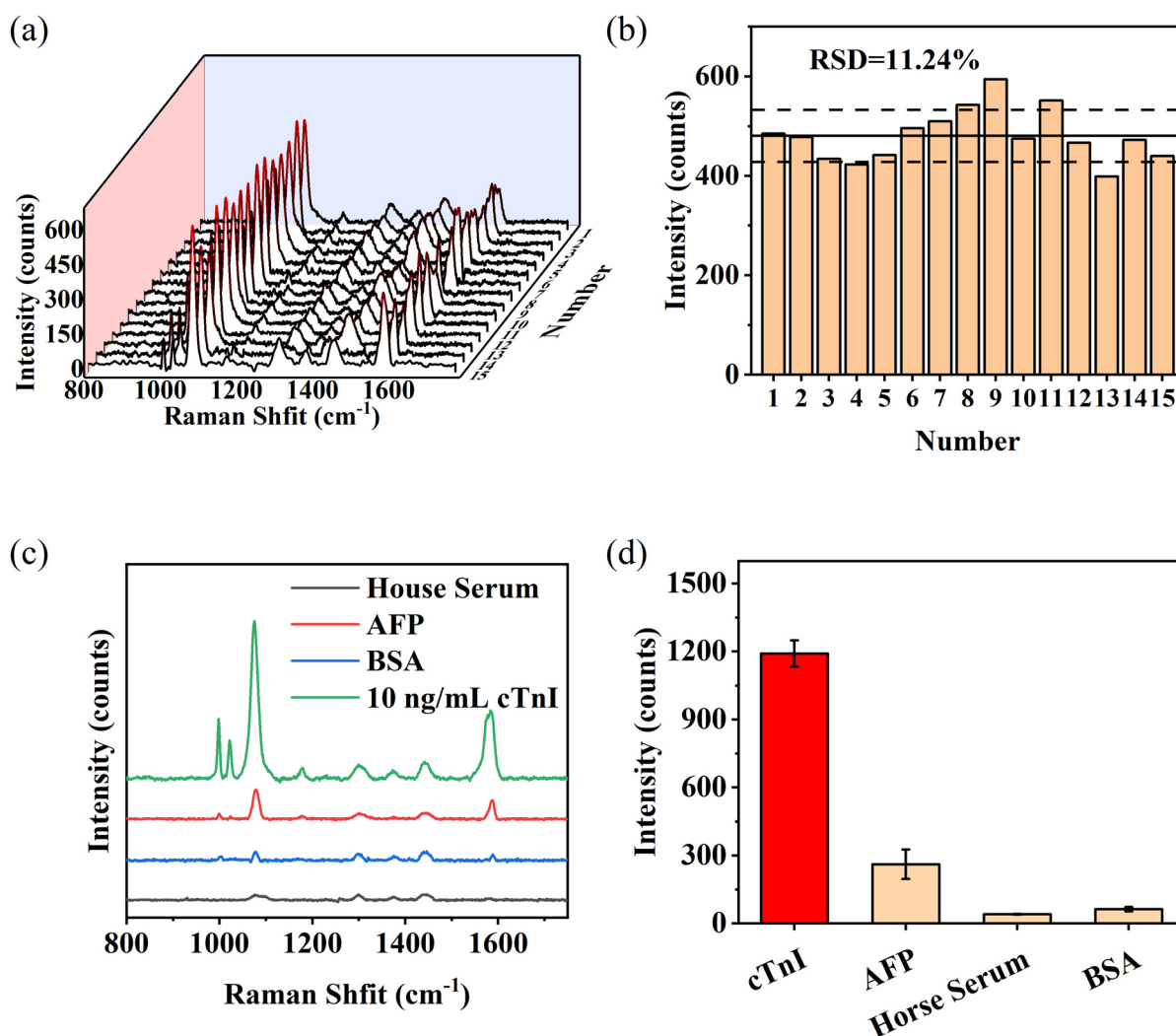

Fig. 6 (a) Raman spectra of 15 random spots on the SERS sensor immersed with the cTnI concentration of 0.1 ng mL^{-1} and (b) their RSD of peak intensities at 1077 cm^{-1}. (c) Raman spectra of cTnI, BSA, AFP, and house serum incubated on the SERS sensor and (d) their peak intensities at 1077 cm^{-1}.

with a moderate decrease in signal intensity (approximately 30%) over the four-month period (Fig S11†).

To verify the specificity of the SERS-based immunoassay platform, we selected AFP, horse serum, and BSA as targets for specificity evaluation. These substances can not only simulate the environment of multiple disease markers that may exist in clinical testing and avoid cross-reactions, but also serve as complex biological matrices to comprehensively assess the anti-interference ability and specificity of the detection method.[34,61,62] The concentration of the target protein was 10 ng mL^{-1}, while those of the interfering proteins were 1 μg mL^{-1}. The Raman intensity of the characteristic peak at 1077 cm^{-1} was used as a reference to evaluate the specificity of the SERS sensor. As shown in Fig. 6(c) and (d), only the AMI biomarker cTnI showed a strong SERS response due to the formation of specific sandwich immunoassay structures. In contrast, the interfering proteins, even at a concentration of 1 μg mL^{-1}, exhibited only weak responses. The results indicate that the SERS-based biosensor possesses high specificity for the target antigen.

Conclusions

In summary, we developed a SERS immunoassay featuring high-density hot spots and excellent reproducibility. Au nanosphere arrays with high uniformity were prepared *via* a three-phase liquid–liquid interfacial self-assembly method, which ensures the even distribution of hot spots and lays the foundation for high reproducibility of the target SERS immunosensor. To further increase the sensitivity, the Au nanosphere arrays were modified and transformed into multi-tipped Au nanostars, which possess intense hot spots and higher Raman enhancement. Compared to the unmodified Au nanosphere array, the SERS signal intensity of the Au nanostar array was significantly enhanced by about 3 times. Using this SERS immunosensor, we successfully detected the cardiac biomarker cTnI with a LOD as low as 9.09 pg mL^{-1}. The SERS immunosensors exhibit high reproducibility, with an RSD of 11.24%, and high selectivity in the presence of other interfering proteins, including AFP, BSA, and Horse Serum. The developed SERS-active immunoassay demonstrates great promise and is anticipated to be practically applied to the early diagnosis of cardiovascular diseases, holding significant potential in the fields of biology and medicine.

Author contributions

The manuscript was written through the contributions of all authors. All authors have given approval for the final version of the manuscript.

Data availability

All data supporting the findings of this study are available within the paper and its ESI.†

Conflicts of interest

There are no conflicts to declare.

Acknowledgements

References

1 M. Ouyang, D. Tu, L. Tong, M. Sarwar, A. Bhimaraj, C. Li, G. L. Cote and D. Di Carlo, *Biosens. Bioelectron.*, 2021, **171**, 112621.

2 J. Liu, Y. Wang, W. Peng, B. Qiu, K.-y. Wong and S. Hu, *Anal. Chim. Acta*, 2025, **1350**, 343800.

3 J. Zhang, H. Liu, B. Xu, S. Huang, R. Liu, J. Zhu, Y. Guo and L. Xu, *Int. J. Polym. Sci.*, 2020, **2020**, 8855550.

4 J. Osredkar, A. Bajrić, H. Možina, L. Lipar and A. Jerin, *Appl. Sci.*, 2024, **14**, 6007.

5 Y. Liu, R. Gao, Y. Zhuo, Y. Wang, H. Jia, X. Chen, Y. Lu, D. Zhang and L. Yu, *Anal. Chim. Acta*, 2023, **1239**, 340673.

6 P. Welsh, D. Preiss, C. Hayward, A. S. Shah, D. McAllister, A. Briggs, C. Boachie, A. McConnachie, S. Padmanabhan and C. Welsh, *Circulation*, 2019, **139**, 2754–2764.

7 H. Yan, X. Tang, X. Zhu, Y. Zeng, X. Lu, Z. Yin, Y. Lu, Y. Yang and L. Li, *Sens. Actuators, B*, 2018, **277**, 234–240.

8 K. Thygesen, J. S. Alpert, A. S. Jaffe, B. R. Chaitman, J. J. Bax, D. A. Morrow, H. D. White and The Executive Group on behalf of the Joint European Society of Cardiology (ESC)/American College of Cardiology (ACC)/American Heart Association (AHA)/World Heart Federation (WHF) Task Force for the Universal Definition of Myocardial Infarction, *Circulation*, 2018, **138**, e618–e651.

9 L. Jiao, L. Zhang, W. Du, H. Li, D. Yang and C. Zhu, *Nanoscale*, 2019, **11**, 8798–8802.

10 G.-R. Han and M.-G. Kim, *Sensors*, 2020, **20**, 2593.

11 G.-R. Han and M.-G. Kim, *Biotechnol. Bioprocess Eng.*, 2019, **24**, 206–214.

12 H. Zhao, E. Su, L. Huang, Y. Zai, Y. Liu, Z. Chen, S. Li, L. Jin, Y. Deng and N. He, *Chin. Chem. Lett.*, 2022, **33**, 743–746.

13 L. Zhao, L. Sun and X. Chu, *TrAC, Trends Anal. Chem.*, 2009, **28**, 404–415.

14 Y. Hu, S. Cheng, L. Chen, L. Xie, H. Fu, Z. Sun, R. Hu, Y. Liu, Z. Wang and B. Z. Tang, *Sens. Actuators, B*, 2024, **408**, 135562.

15 L.-G. Chen, L. Sun, N.-N. Wu, B.-B. Tao and H.-B. Wang, *Anal. Chim. Acta*, 2023, **1279**, 341843.

16 S. Roth, O. Hadass, M. Cohen, J. Verbarg, J. Wilsey and A. Danielli, *Small*, 2019, **15**, 1803751.

17 H. Han, C. Wang, X. Yang, S. Zheng, X. Cheng, Z. Liu, B. Zhao and R. Xiao, *Sens. Actuators, B*, 2022, **351**, 130897.

18 B. Zhang, Y. Zhang, W. Liang, X. Yu, H. Tan, G. Wang, A. Li, J. Jin and L. Huang, *RSC Adv.*, 2017, **7**, 2486–2493.

19 X. Qiao, K. Li, J. Xu, N. Cheng, Q. Sheng, W. Cao, T. Yue and J. Zheng, *Biosens. Bioelectron.*, 2018, **113**, 142–147.

20 X. Qin, D. Li, X. Qin, F. Chen, H. Guo, Y. Gui, J. Zhao, L. Jiang and D. Luo, *View*, 2024, **5**, 20240025.

21 A. I. Pérez-Jiménez, D. Lyu, Z. Lu, G. Liu and B. Ren, *Chem. Sci.*, 2020, **11**, 4563–4577.

22 P. M. Pancorbo, H. Zhang, X. Yu, T.-H. Xiao and K. Goda, *Europhys. Lett.*, 2022, **136**, 34001.

23 N. Lyu, A. Hassanzadeh-Barforoushi, L. M. Rey Gomez, W. Zhang and Y. Wang, *Nano Convergence*, 2024, **11**, 22.

24 D. Lu, Y. Chen, L. Ke, Z. Huang, Y. Lu and J. Wang, *Chem. Eng. J.*, 2025, **503**, 158491.

25 L. C. Wang, Y. C. Kuo, Y. T. Kuo, K. L. Chang, Y. C. Chen, W. J. Wang, M. Y. Hung, F. Y. Hsu, P. Aich and Y. W. Lin, *Adv. Mater.*, 2025, 2417950.

26 G. Devitt, K. Howard, A. Mudher and S. Mahajan, *ACS Chem. Neurosci.*, 2018, **9**, 404–420.

27 J. Sun, Z. Shi, L. Wang, X. Zhang, C. Luo, J. Hua, M. Feng, Z. Chen, M. Wang and C. Xu, *Talanta*, 2023, **261**, 124677.

28 S. Lee, H. Dang, J.-I. Moon, K. Kim, Y. Joung, S. Park, Q. Yu, J. Chen, M. Lu and L. Chen, *Chem. Soc. Rev.*, 2024, **53**, 5394–5427.

29 H. Zhang, J. Y. Dong, X. Tang, N. Kishimoto, Y. Deng, H. Zhang, X. Yu, Y. Nakagawa, S. T. Zhang and Y. Kagotani, *Adv. Opt. Mater.*, 2025, **13**, 2402673.

30 H. Zhang, H. Wang, Y. Huang, B. Wang, Q. Xiang, L. Xiao, Y. Shu, L. Ying, S. Wang and Y. Ma, *J. Phys. Chem. Lett.*, 2025, **16**, 2097–2103.

31 X. Yu, X. Tang, J.-Y. Dong, Y. Deng, M. Saito, Z. Gao, P. M. Pancorbo, M. Marumi, W. Peterson and H. Zhang, *ACS Nano*, 2024, **18**, 30987–31001.

32 Z. Cheng, R. Wang, Y. Xing, L. Zhao, J. Choo and F. Yu, *Analyst*, 2019, **144**, 6533–6540.

33 R. Gao, Y. Mao, C. Ma, Y. Wang, H. Jia, X. Chen, Y. Lu, D. Zhang and L. Yu, *ACS Appl. Mater. Interfaces*, 2022, **14**, 55414–55422.

34 T. Wang, H.-S. Tan, L.-X. Zhao, M. Liu and S.-S. Li, *Sens. Actuators, B*, 2024, **412**, 135804.

35 H. Lee, H. Youn, A. Hwang, H. Lee, J. Y. Park, W. Kim, Y. Yoo, C. Ban, T. Kang and B. Kim, *Nanomaterials*, 2020, **10**, 1402.

36 E.Ç Kayiş, H. Torul, S. A. Sazaklıoğlu, H. Çelikkan, H. K. Ensarioğlu, B. H. Gumus, H. S. Vatansever and U. Tamer, *Sens. Actuators, B*, 2025, **426**, 137103.

37 P. Dai, Z. Zhang, X. Hou, L. Ouyang and L. Zhu, *Talanta*, 2021, **234**, 122651.

38 H. K. Lee, Y. H. Lee, C. S. L. Koh, G. C. Phan-Quang, X. Han, C. L. Lay, H. Y. F. Sim, Y.-C. Kao, Q. An and X. Y. Ling, *Chem. Soc. Rev.*, 2019, **48**, 731–756.

39 A. Kaminska, O. Inya-Agha, R. J. Forster and T. E. Keyes, *Phys. Chem. Chem. Phys.*, 2008, **10**, 4172–4180.

40 Y. Wang, D. Li, Y. Sun, L. Zhong, W. Liang, W. Qin, W. Guo, Z. Liang and L. Jiang, *ACS Appl. Mater. Interfaces*, 2020, **12**, 6176–6182.

41 B. Lu, K. Vegso, S. Micky, C. Ritz, M. Bodik, Y. M. Fedoryshyn, P. Siffalovic and A. Stemmer, *ACS Nano*, 2023, **17**, 12774–12787.

42 X. Li, T. Zhang, Z. Chen, J. Yu, A. Cao, D. Liu, W. Cai and Y. Li, *Small*, 2022, **18**, 2105045.

43 X. Lin, G. Fang, Y. Liu, Y. He, L. Wang and B. Dong, *J. Phys. Chem. Lett.*, 2020, **11**, 3573–3581.

44 Y. Zheng, X. Zhong, Z. Li and Y. Xia, *Part. Part. Syst. Charact.*, 2014, **31**, 266–273.

45 Q. Ruan, L. Shao, Y. Shu, J. Wang and H. Wu, *Adv. Opt. Mater.*, 2014, **2**, 65–73.

46 Z. Jin, Q. Yue, W. Duan, A. Sui, B. Zhao, Y. Deng, Y. Zhai, Y. Zhang, T. Sun and G. P. Zhang, *Adv. Sci.*, 2022, **9**, 2104935.

47 Y. Yang, J. Zhu, J. Zhao, G.-J. Weng, J.-J. Li and J.-W. Zhao, *ACS Appl. Mater. Interfaces*, 2019, **11**, 3617–3626.

48 L. Zhou, Y. Liu, F. Wang, Z. Jia, J. Zhou, T. Jiang, L. Petti, Y. Chen, Q. Xiong and X. Wang, *Talanta*, 2018, **188**, 238–244.

49 G. Braun, I. Pavel, A. R. Morrill, D. S. Seferos, G. C. Bazan, N. O. Reich and M. Moskovits, *J. Am. Chem. Soc.*, 2007, **129**, 7760–7761.

50 T. Jiang, L. Zhang and J. Zhou, *Analyst*, 2014, **139**, 5893–5900.

51 D. Luo, C. Yan and T. Wang, *Small*, 2015, **11**, 5984–6008.

52 X. Li, X. Liu and X. Liu, *Chem. Soc. Rev.*, 2021, **50**, 2074–2101.

53 Y. Li, D. Liang, R. Wang, S. Yang, W. Liu, Q. Sang, J. Pu, Y. Wang and K. Qian, *Small*, 2024, **20**, 2405318.

54 M. A. Boles, M. Engel and D. V. Talapin, *Chem. Rev.*, 2016, **116**, 11220–11289.

55 J.-F. Li, Y.-J. Zhang, S.-Y. Ding, R. Panneerselvam and Z.-Q. Tian, *Chem. Rev.*, 2017, **117**, 5002–5069.

56 Y. Gao, J. Wang, W. Wang, T. Zhao, Y. Cui, P. Liu, S. Xu and X. Luo, *Anal. Chem.*, 2021, **93**, 2480–2489.

57 H. Liu, Y. Xu, Y. Qin, W. Sanderson, D. Crowley, C. H. Turner and Y. Bao, *J. Phys. Chem. C*, 2013, **117**, 17143–17150.

58 S. Ge, M. Ran, Y. Mao, Y. Sun, X. Zhou, L. Li and X. Cao, *Analyst*, 2021, **146**, 5326–5336.

59 R. Gao, F. Chen, D. Yang, L. Zheng, T. Jing, H. Jia, X. Chen, Y. Lu, S. Xu and D. Zhang, *Sens. Actuators, B*, 2022, **369**, 132378.

60 M. Zhang, X. Li, J. Pan, Y. Zhang, L. Zhang, C. Wang, X. Yan, X. Liu and G. Lu, *Biosens. Bioelectron.*, 2021, **190**, 113421.

61 J. Liu, G. Ruan, W. Ma, Y. Sun, H. Yu, Z. Xu, C. Yu, H. Li, C.-W. Zhang and L. Li, *Biosens. Bioelectron.*, 2022, **198**, 113823.

62 S. A. Kitte, T. Tafese, C. Xu, M. Saqib, H. Li and Y. Jin, *Talanta*, 2021, **221**, 121674.